UNIVERSITY OF CALIFORNIA
RIVERSIDE

Statistical Correlations in Exoplanet Eccentricities

A Thesis submitted in partial satisfaction
of the requirements for the degree of

Master of Science

in

Earth and Planetary Sciences

by

Alma Y. Ceja

December 2022

Thesis Committee:

Professor Stephen Kane, Chairperson
Professor Andrew Ridgwell
Professor Robert Allen

The Thesis of Alma Y. Ceja is approved:

Committee Chairperson

University of California, Riverside

Acknowledgments

I am grateful to the members of the Planetary Research Laboratory. I'd like to especially thank Dr. Kimberly Bott and Dr. Tara Fetherholf for all of their help in both performing the following analyses and writing this manuscript. Finally, I'd like to express my gratitude to my advisor and friend, Dr. Stephen Kane, without whose support I would not have had the opportunity to embark on this amazing journey. Thank you.

To my mother, my father, and my brothers, for their infinite love and support.

ABSTRACT OF THE THESIS

Statistical Correlations in Exoplanet Eccentricities

by

Alma Y. Ceja

Master of Science, Graduate Program in Earth and Planetary Sciences
University of California, Riverside, December 2022
Professor Stephen Kane, Chairperson

Exoplanet discoveries have proved numerous planetary system orbital configurations, including the discovery of exoplanets on highly elliptical orbits. The most eccentric planet in our own solar system, Mercury, exhibits an eccentricity of only 0.205, and Earth's eccentricity is a mere 0.017. By comparison, exoplanets have been discovered with orbital eccentricities ranging from zero to 0.956 (HD20782, Kane et al. 2016). Because the eccentricity of a planet is largely responsible for its received stellar insolation, and thus its climate and habitability, it is crucial to be able to model this value in the absence of measurements. The prevailing theory explaining the enhanced ellipticity observed is that dynamical instabilities can cause eccentric orbits by planet-planet scattering where one planet is ejected from the system and, in accordance with the law of conservation of angular momentum, the other is left to undertake an eccentric orbit (Carrera et al. 2019)..

Furthermore, it has been observed that low-mass stars are less likely to harbor giant planets than massive stars Nielsen et al. (2019). Thus, the higher frequency of giant planets around more massive stars may lead to interactions whose signatures remain

in the angular momentum of eccentric orbits. This work aims to connect eccentricity distributions to planet formation and dynamical evolution models by investigating possible correlations of eccentricity with host star mass and chemical composition. I describe series of statistical data analysis techniques, including contour modeling, frequency analyses, and Beta-distribution modeling, to identify patterns in the distribution of exoplanet eccentricities and correlations with host star properties. Such correlations may have significant implications for the relative occurrence rate of terrestrial planets in systems where giant planets are more likely to exclude their orbital integrity.

Contents

List of Figures

Chapter 1

Introduction

The population of confirmed exoplanets has revealed a diversity of orbital configurations ranging from short-period gas giants (<10 days, e.g. WASP- 4b, (Wilson et al. 2008)) to free-floating rogue planets (e.g. Cha110913- 773444, Luhman et al. (2005)). We now have constraints on exoplanet discoveries that allow us to explore broad topics regarding statistics and demographics (e.g. Figure 1.1). In particular, interactions between planets and their orbital evolution can be tied to formation processes and the stellar disk composition. An indicator of these interactions is the observed orbital eccentricity of exoplanets. One especially astonishing discovery was that of exoplanets on highly elliptical orbits. The most eccentric planet in our own solar system, Mercury, exhibits an eccentricity of only 0.205, and Earth's eccentricity is a mere 0.017. By comparison, exoplanets have been discovered with orbital eccentricities ranging from zero (perfectly circular) to 0.956 (nearly linear, HD20782, Kane et al. (2016)). We've even discovered planets with eccentricities of 1.0 (Liu et al. (2013))! These exoplanets, termed 'rogue' or 'free-floating' planets, are not

gravitationally bound in orbit to a star. Instead, they travel in linear trajectories in space and are presumed to have been entirely ejected from their home system due to extreme interactions with other, larger bodies found within their original planetary system.

The prevailing theory is that dynamical instabilities can cause eccentric orbits by planet-planet scattering where one planet is ejected from the system and, in accordance with Newton's Third Law of the conservation of angular momentum, the other is left to undertake an eccentric orbit (Chatterjee et al. (2008)). Here, a statistical effort is made to identify preliminary patterns in the distribution of exoplanet eccentricities. It is of importance to note that the current pool of confirmed exoplanets is biased to observational limits, and this unavoidable bias propagates through this analysis. Selection methods are applied in an attempt to offset the observational biases. The resulting sample is analyzed with a series of non-parametric statistical tests including frequency distributions, density contours, and quartile summaries.

The aim of this work is two-fold: to generate a model to predict the eccentricity of exoplanets orbiting specific star-types and to elucidate the statistical correlations present in the distribution of exoplanet eccentricities.

1.1 Keplerian Orbits

A Keplerian orbit describes the motion of one body relative to another. In celestial mechanics, as in all orbiting systems, both the star and planet orbit a common center of mass, the barycenter. The orbit of a body around this barycenter can be circular, elliptical, parabolic, hyperbolic, or linear. Thus, a Keplerian orbit is said to be a solution of the special

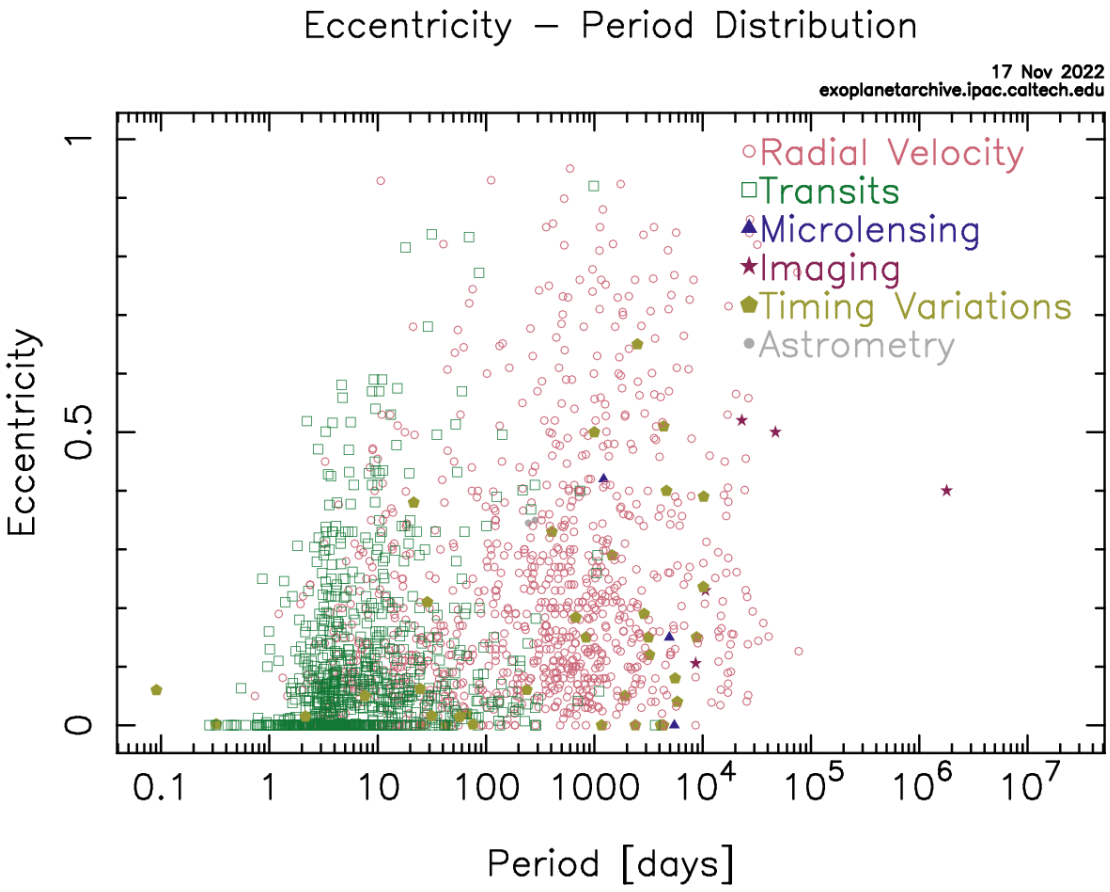

Figure 1.1 The distribution of measured exoplanet eccentricities and corresponding orbital periods shown color-grouped by discovery method (n=1515). This plot, which is pre-generated by the NASA Exoplanet Archive (exoplanetarchive.ipac.caltech.edu), was downloaded on 19 November 2022.

case of the 'two-body problem', also known as the Kepler problem. Three-dimensional Keplerian orbits can be parameterized into seven orbital elements (a, e, P, t_p, i, Ω, and ω), where a is the star-planet separation, e is the planet eccentricity, P is the planet's orbital period, and t_p is the planet's position along its orbit at a particular reference time. The angles i, Ω, and ω represent the projection of the true orbit into the observed (apparent) orbit. The angle i specifies the orbital inclination with respect to a reference plane. The angle Ω represents the longitude of the ascending node measured in the reference plane. This is the node where the measured object moves away from the observer through the plane of reference. Finally, ω is the argument of pericenter measured in the orbital plane and in the direction of motion (Figure 1.2, (Perryman 2018)).

The Kepler problem can be solved mathematically with Equations 1.1, 1.2, 1.3, and 1.4, where r is the star-planet separation, $E(t)$ is the eccentric anomaly, $M(t)$ is the mean anomaly, and n is the planet's mean motion.

$$r = \frac{a(1-e^2)}{1+e\cos v(t)} \tag{1.1}$$

$$cosv(t) = \frac{cosE(t)-3}{1-e\cos E(t)} \tag{1.2}$$

$$n = \frac{2\pi}{P} \tag{1.3}$$

$$M(t) = n(t-t_p) \tag{1.4}$$

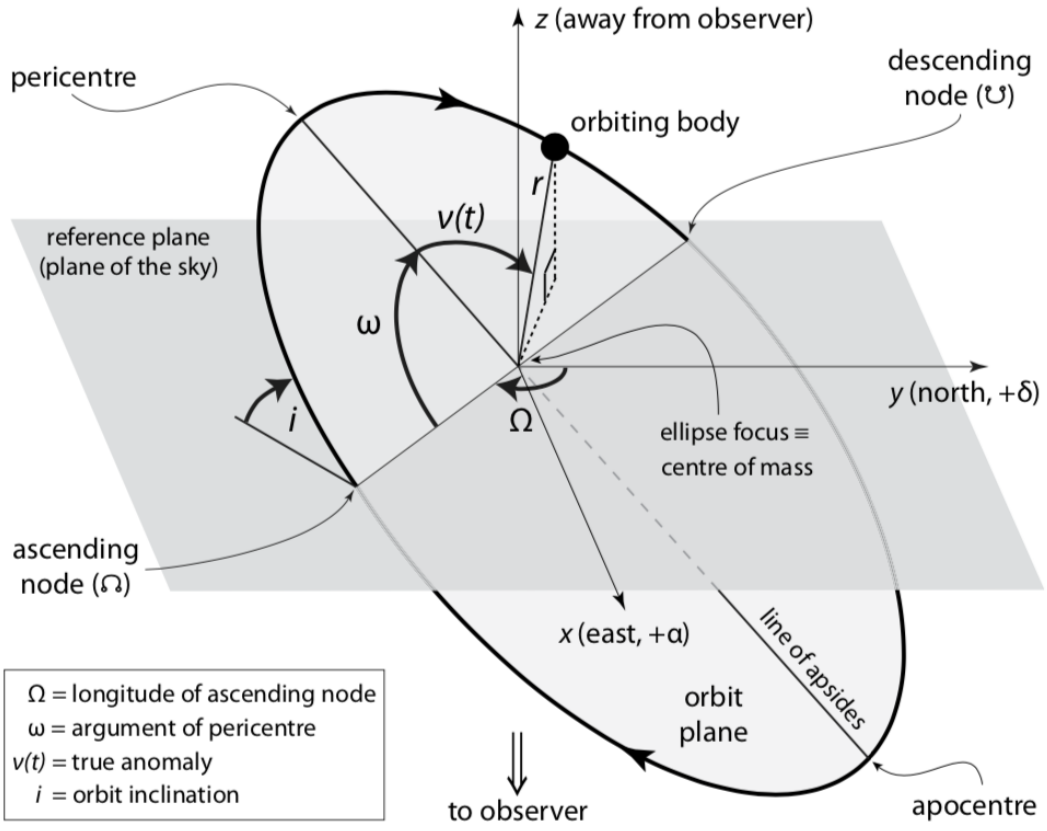

Figure 1.2 An elliptical orbit in three dimensions. The reference plane is tangent to the celestial sphere, i is the inclination of the orbit plane, and the nodes define the intersection of the orbit and reference planes. Ω is the longitude of the ascending (receding) node, measured in the reference plane. ω is the fixed angle defining the object's argument of pericenter relative to the ascending node. The true anomaly, $v(t)$, is the time-dependent angle characterizing the object's position along the orbit. The right-handed x y z coordinate system has x towards east (increasing a), y towards north (increasing δ), and z away from the observer, consistent with the Thiele–Innes constants. The reference axis, y, contrasts with the use of x, the vernal equinox, as adopted for the solar system (Perryman 2018).

1.2 Observables and Data

Planets discovered with radial velocity (RV) techniques where eccentricity is measured provide a huge statistical sample to study the distribution of these parameters, all of which relate to planet formation and orbital evolution. Initially, a large sample of planetary eccentricities were measured with the radial velocity method (Shen & Turner 2008). Upon the retrieval of data from the Kepler space telescope, the number of eccentricity measurements skyrocketed by transit observations (Kane et al. 2012). Additionally, a great deal of measurements have been acquired from direct imaging techniques (Bowler et al. 2020). This analysis primarily makes use of three types of observables: orbital eccentricity, stellar mass, and stellar metallicity (iron abundance, $[Fe/H]$).

Orbital eccentricity (e) can be calculated from the equation for RV semi-amplitude (K), Equation 1.5, where orbital period (P), orbital inclination (i), and semi-major axis (a) are known.

$$K = \frac{2\pi}{P} \frac{a_* \sin i}{\sqrt{1-e^2}} \tag{1.5}$$

Stellar mass models generated from calculations of stars in multi-star systems (i.e. binary or ternary systems) where there is a perturbing body, which generates stellar mass models. These stellar mass models are then applied to estimate stars in single systems based on their spectral properties.

The composition of a star, or stellar metallicity ($[Fe/H]$) is simply determined from its spectrum, which unlocks the composition and abundance from spectral line width and strength.

1.3 Planet Formation

The currently accepted method by which planets are created is described in the core accretion theory, in which planets are thought to form simultaneously with their stars (Mordasini et al. 2007). The process begins with an interstellar hydrogen and helium cloud which contracts as a result of self-gravity. The cloud is flattened, with the densest region found at the center. The high temperatures and pressures at the core trigger thermonuclear fusion, igniting the central protostar. Grains of orbiting dust collide and accrete into planetesimals which grow in coplanar orbits to form planetary embryos. The disk's thermal gradient, with a hot core and cooler edges, dictates planetary composition. The hot core is dense with elements of high melting point, including iron. The cool edges contain frozen species like water, methane, and ammonia. On the outer edges of the system, gas giant planets quickly accrete gas envelopes before the gaseous disk disappears. These giants then scatter or accrete the remaining planetesimals and embryos. Some of these bodies grow sufficiently massive to gravitationally attract any remaining matter in their 'neighborhood'. Thus, a typical planetary system, like our own Solar System, generally features rocky planets orbiting close to the star, and gaseous outer planets orbiting further away (Bodenheimer & Pollack 1986; Mizuno et al. 1978; Perri & Cameron 1974).

However, the system continues to evolve following initial formation. As planets interact with disk debris and other small bodies, they can migrate and alter their semi-major axis. Thus, larger planets can gravitationally scatter smaller bodies. As the two bodies exchange angular momentum, the smaller planet is left to undertake an eccentric

orbit. This planet-planet scattering is believed to be the primary source of high exoplanet eccentricities (Carrera et al. 2019; Jurić & Tremaine 2008; Kane & Raymond 2014).

1.4 Implications for Habitability

Earth is believed to have a low-variability climate largely due to its nearly circular orbit. Because of its low eccentricity, Earth receives roughly the same amount of average stellar insolation across the astronomical year (Dressing et al. 2010). Thus, although we experience seasonal variability due to our 23.4° obliquity, the average regional temperature is negligibly influenced by its star-planet separation.

By comparison, within our own solar system, the dwarf planet Pluto features an eccentricity of 0.25. This variability in star-planet separation leads to an interesting effect in Pluto's atmosphere. During perihelion, its atmosphere exists as a tenuous layer of primarily nitrogen in gaseous form. However, during aphelion, at its farthest distance from the sun, Pluto's atmosphere collapses and freezes over due to its great distance from our star resulting in 25% lower stellar insolation (Bertrand & Forget 2017). Expanding this knowledge from the confines of our solar system to the great many potentially terrestrial exoplanets on various eccentric orbits, it is clear that eccentricity is key in unlocking the climates and elucidating the habitability of planets elsewhere (Kane & Gelino 2012; Way & Georgakarakos 2017).

Primary targets for habitability are terrestrial planets orbiting within the habitable zone of their system, and eccentricity measurements of extrasolar planets show that small planets feature largely circular orbits (Van Eylen et al. 2019; Mills et al. 2019). A

highly eccentric planet in the presence of a potentially habitable exoplanet is likely to largely interfere with its orbit (Kane & Blunt 2019), and a would-be temperate climate of a terrestrial world (Kane & Torres 2017). Thus, in determining the habitability of a terrestrial planet within the habitable zone, it is crucial to predict the orbital dynamics of said planet, beginning with its orbital eccentricity (Kipping 2013).

Chapter 2

Methods and Results

In this chapter, describe the methods that were performed and the accompanying results. First, I discuss the data acquisition from the NASA Exoplanet Archive. These data are constrained to offset observational bias. The correlations between eccentricity and both stellar metallicity (iron abundance, $[Fe/H]$) and stellar mass are then examined within a series of statistical analyses including frequency distribution and non-parametric quartile analysis. Finally, I discuss the generated prediction models between stellar parameters and eccentricity.

2.1 Data Acquisition

A table of parameters for confirmed exoplanets meeting the four constraints described below was downloaded from the NASA Exoplanet Archive on 8 February 2022. Exoplanet parameters include orbital eccentricity (e), upper and lower error limits for orbital eccentricity, stellar mass (M), and stellar iron abundance (*[Fe/H]*). Stellar iron abundance

is used as a proxy for stellar composition. Eccentricity values equal to zero ($e = 0$) or lacking error limits are assumed to be fixed in a Keplerian Orbital fit. Thus, because the goal of this study is to sample the most accurate values of eccentricities which were allowed to float as free parameters, exoplanets with $e = 0$ or no error limits were excluded from this table. Further, in order to explore correlations between exoplanet eccentricity and host star composition, exoplanets without a measured stellar mass or stellar iron abundance were also excluded from this analysis. Applying all of these constraints together to the total population of $N = 4,914$ confirmed exoplanets (at the time of this analysis) produced a sample of $n = 890$ exoplanets (Figure 2.1).

2.2 Statistical Analyses

Various statistical techniques were applied in an attempt to elucidate how the parameters of host star stellar mass and stellar iron metallicity correlate with the eccentricities of orbiting exoplanets. These include frequency distribution analysis, quantile analysis, and bivariate predictive density contour modeling. For all analyses, the statistical software R was used within the integrated development environment (IDE), RStudio. All figures were generated using the R data visualization package, ggplot2.

2.2.1 Exoplanet Distributions

Within the sample, exoplanet eccentricities range from 0.01 to 0.95 with a mean of $e = 0.215$, and frequency increasing towards lower eccentricities (Figure 2.2, dark gray). This frequency distribution is a direct consequence of the applied constraints described

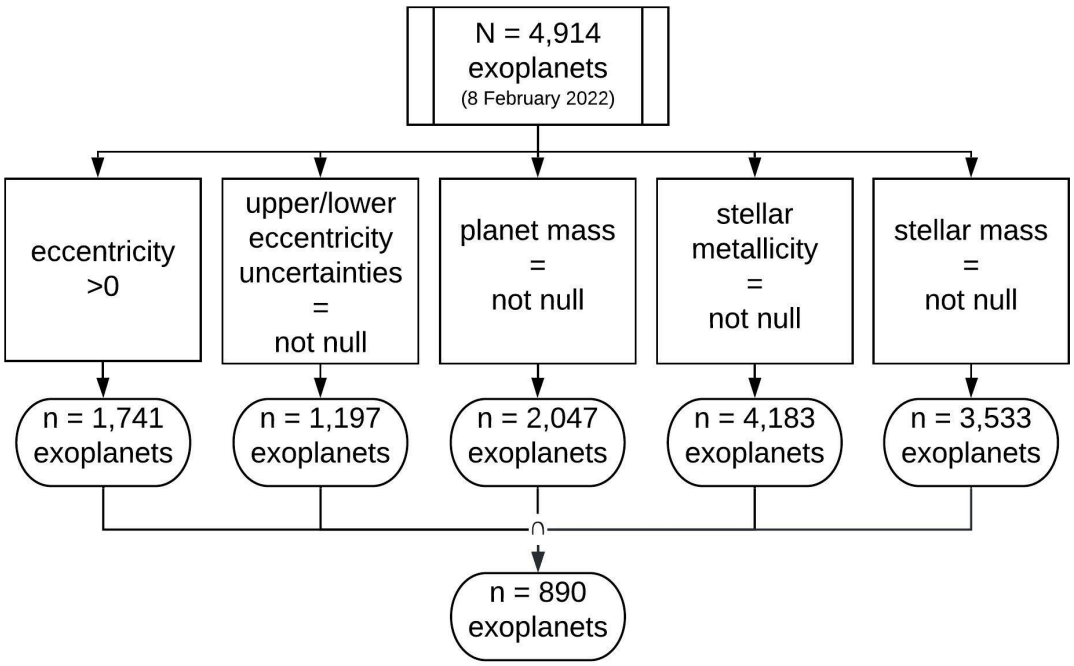

Figure 2.1 Flowchart depicting the individual constraints imposed on the total population of confirmed exoplanets from the NASA Exoplanet Archive on 8 February 2022 (N=4,914 exoplanets). Imposing the constraints of 1) planets with orbital eccentricity greater than zero ($e > 0$), 2) planets with a reported upper or lower error on orbital eccentricity, 3) planets orbiting a host star with a reported stellar mass (M = not null), and 4) planets orbiting a host star with reported stellar iron abundance ($[Fe/H]$ = not null) on the total population of confirmed exoplanets produced a sample of $n = 890$ exoplanets for analysis.

in the previous section. Of these exoplanets, those with potentially rocky compositions exhibit a much smaller distribution with orbital eccentricities from 0.01 to 0.34 (Figure 2.2). This distribution results from the boundary between rocky and gaseous planets. Here, a conservative boundary of planet mass less than 2.3 earth masses was selected. One fundamental challenge in exoplanet science is to understand the boundary between rocky and gaseous planets, particularly because we have no direct analogs of that boundary in our solar system. This is key as the planetary mass plays a critical role in determining the dynamical evolution of the whole system (the distribution of planetary masses used in this analysis is illustrated in Figure 2.3). Thus, because a goal of this study is to illustrate the frequent planet-planet interactions of giant planets, rocky exoplanets are highlighted.

Note the distribution of stellar masses here (Figure 2.4) is not representative of the entire exoplanet population. Due to target selection survey design, low mass stars are more commonly observed than high mass stars. This is because FGK-type, solar-like stars are easier to measure with RV techniques. On the hotter end of the stellar spectrum, A-type (more massive, hotter stars) lose spectral lines according to the Saha equation. That is, with increasing temperature, spectral lines become stronger until at some point, they disappear. At these high temperatures, hydrogen becomes ionized, losing electrons, and thus does not experience transitions between quantum energy levels, producing a lack of spectral emission lines. On the other hand, young and hot M-type stars have no shortage of spectral lines. However, they are rapid rotators, which results in line broadening of their spectrum. This causes spectral lines to blur as they extend over a range of frequencies. Further, an M-star's

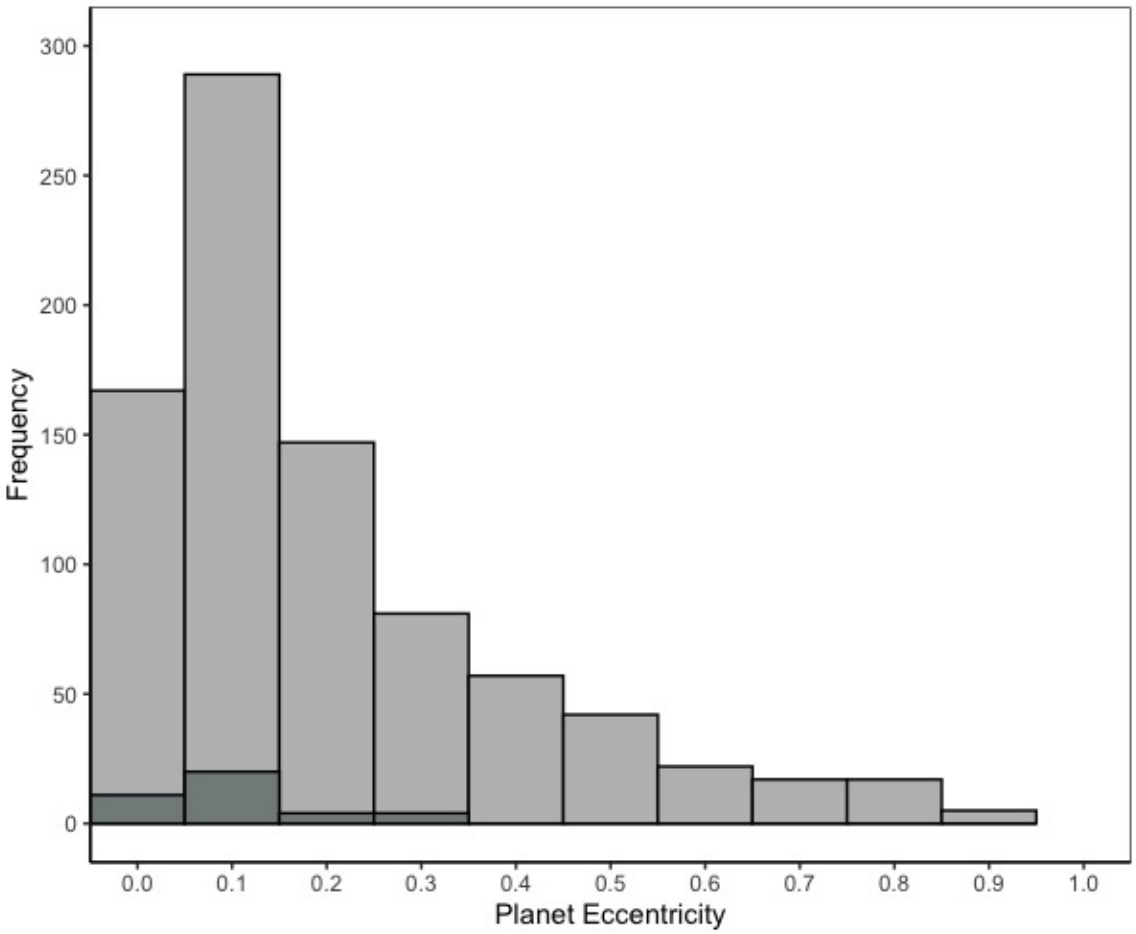

Figure 2.2 Frequency distribution histogram of exoplanet eccentricities of both the entire sample used in this analysis (light gray, $n = 890$ exoplanets, $e_{min} = 0.01$, $e_{max} = 0.95$, $e_{mean} = 0.215$, $e_{median} = 0.149$, $e_{mode} = 0.04$), and the subset of rocky exoplanets ($R_p < 2R_\oplus$, dark gray, $n = 33$, $e_{min} = 0.01$, $e_{max} = 0.34$, $e_{mean} = 0.123$, $e_{median} = 0.1$, $e_{mode} = 0.1$) within the sample. Note, in both distributions, the frequency increases towards smaller eccentricities.

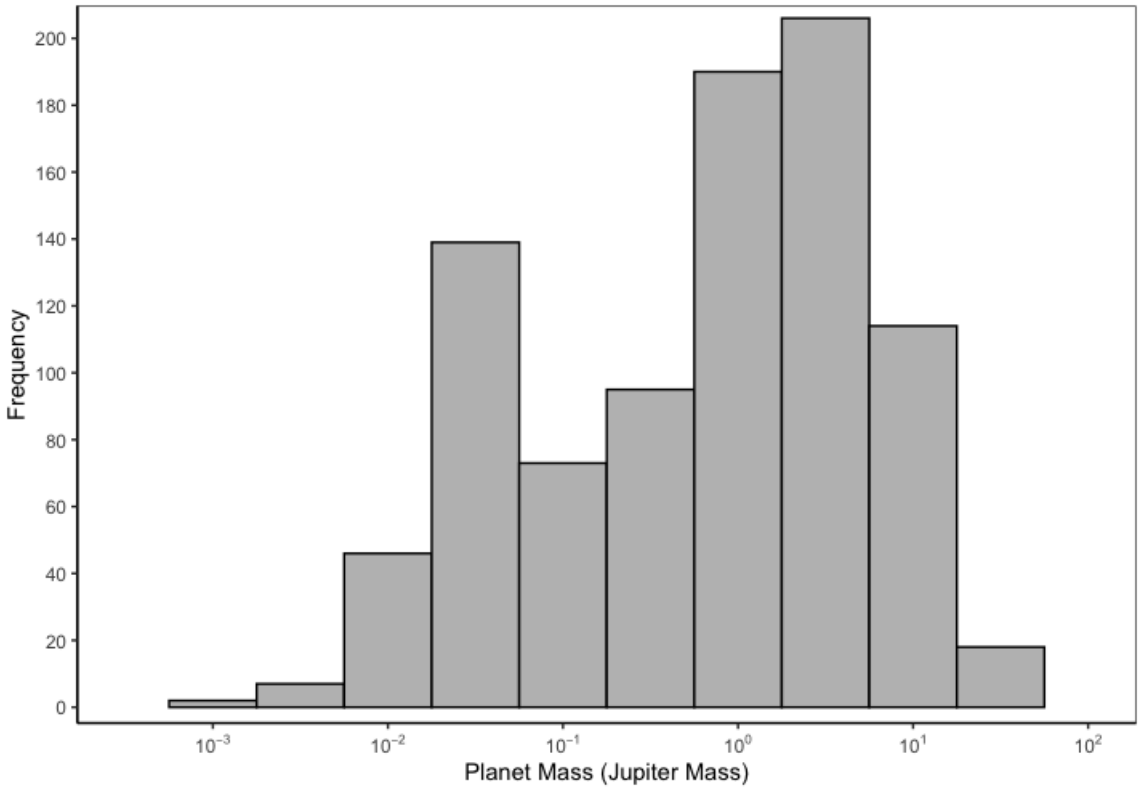

Figure 2.3 Frequency distribution of exoplanet masses (M_p) in Jupiter masses (M_J) used in this analysis ($n = 890$ exoplanets, $M_{p(mean)} = 2.69M_J$, $M_{p(min)} = 0.0009M_J$, $M_{p(max)} = 55.59M_J$, $M_{p(median)} = 0.92M_J$, $M_{p(mode)} = 0.82M_J$.

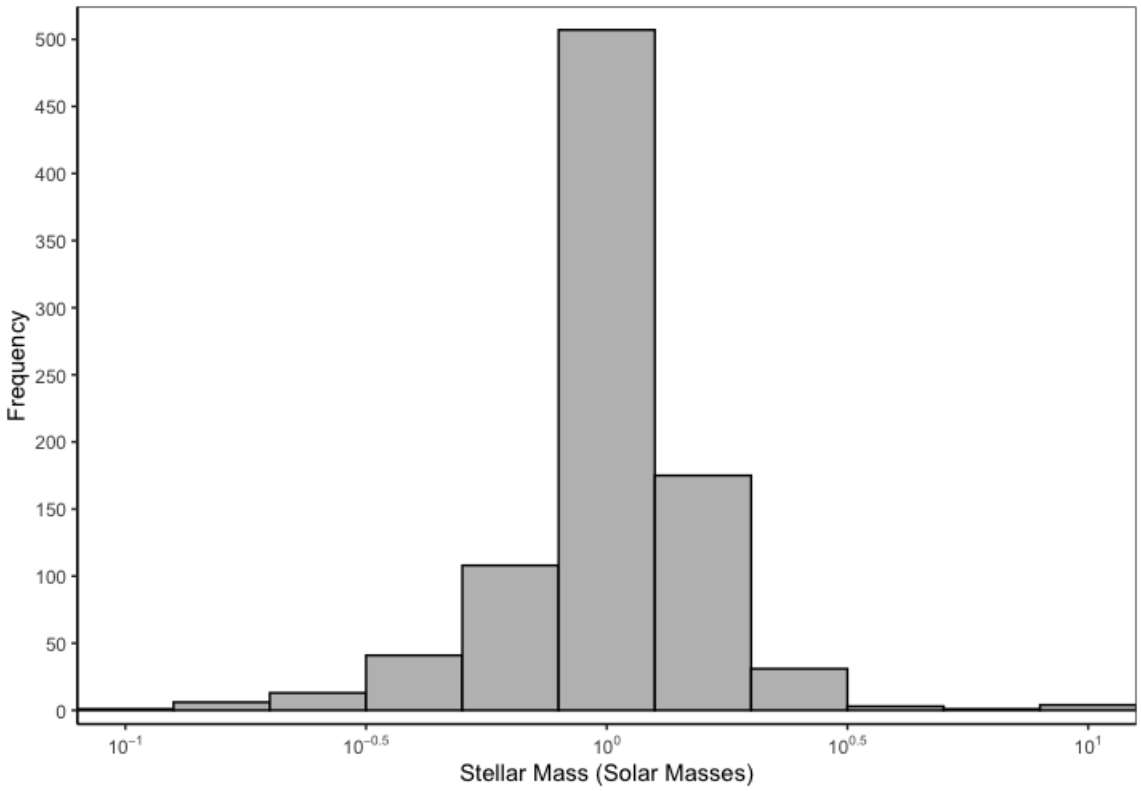

Figure 2.4 Frequency distribution of exoplanet host star stellar masses used in this analysis ($n = 687$ stars, $M_{mean} = 1.07M_{\odot}$, $M_{min} = 0.12M_{\odot}$, $M_{max} = 3.7M_{\odot}$, $M_{median} = 1.03M_{\odot}$, $M_{mode} = 0.94M_{\odot}$).

convective atmosphere results in numerous stellar spots, making it difficult to measure with RV techniques.

A star's metallicity is often defined by its total iron content. This is because iron is among the easiest elements to observe as it emits in the visible spectrum. The stellar metallicity ([Fe/H]) distribution is roughly normal and negatively skewed, peaking at 0.0 dex. This analysis addresses the hypothesis that stars with greater metallicities will produce

more large planets, and that these large planets will induce more planet-planet interactions resulting in systems with higher eccentricities. Stars are grouped by metallicity in either Population I (metal-rich), Population II (metal-poor), and Population III (extremely metal-poor). Due to their formation early on in the history of the Universe when few metals had yet to be created, older stars are naturally metal-poor and fall into either the Population II or Population III category of stars. Younger stars, on the other hand, will exhibit naturally higher metallicities and fall into the Population I category due to their forming later in the Universe's history, after the ample production of metals. Stellar metallicity is also a function of the star's location within the galaxy. For example, stars formed in denser regions will exhibit higher metallicities, where stars formed in thin regions will have lower metallicities. The distribution of stellar metallicities in (Figure 2.5) is a true distribution.

2.2.2 Exoplanet Multiplicity

The relationship between exoplanet eccentricity and exoplanet system multiplicity is displayed using box plots (Figure 2.6). Note systems in binary or ternary star systems were excluded from the sample. Additionally, it is possible and highly probable that the systems represented by the sample of exoplanets here is incomplete as only detected exoplanets are shown. However, although incomplete, considering the sample as is there is a clear trend showing that the range of exoplanet eccentricities is inversely proportional to the number of exoplanets within a system. That is, systems with only one detected planet feature more planets on highly elliptical orbits whereas those with six planets, for example, feature planets with strictly more circular orbits. This data may be indicative of the proposed

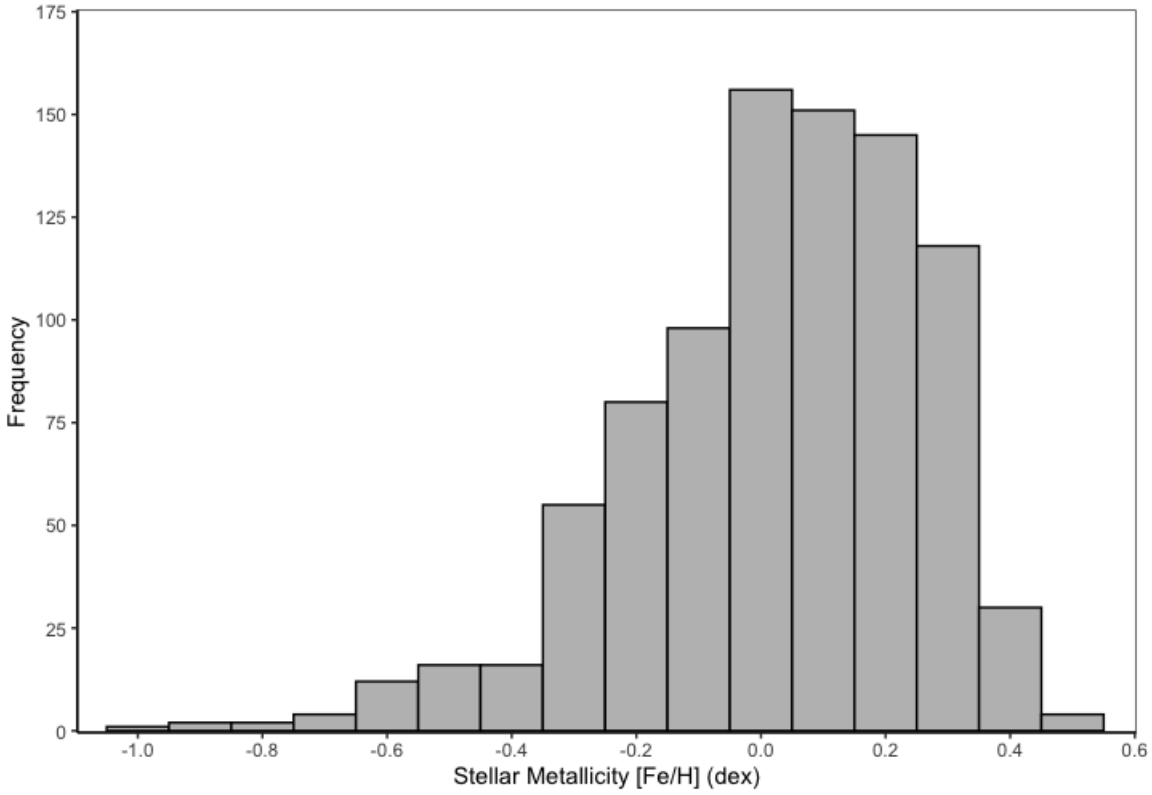

Figure 2.5 Frequency distribution of exoplanet host star stellar iron metallicities ($[Fe/H]$) used in this analysis ($n = 687$ stars, $[Fe/H]_{mean} = 0.325dex$, $[Fe/H]_{min} = -0.89dex$, $[Fe/H]_{max} = 0.0.69dex$, $[Fe/H]_{median} = 0.06dex$, $[Fe/H]_{mode} = 0.0dex$).

planet-planet scattering theory describing system architecture. That is, it is possible that large planets within a system undertake the angular momentum of smaller planets which have been ejected due to planet-planet interactions.

2.2.3 Beta Distribution Modeling

In an attempt to elucidate the proper distribution for each the gaseous and rocky planets, a beta distribution fit was applied to each respective group. This was accomplished using the library Rfast within the R environment (Figure 2.7). For comparison, the entire sample of exoplanets was also fit with the same distribution. Here, the gaseous planet fit nearly identically replicates that of the entire sample. In contrast, the sample of rocky planets produces a beta distribution fit that completely differs from both the gaseous sample and the entire sample, with a turnover point near e=0.1. As in the previous section, this feature could be indicative of the proposed planet-planet scattering theory. Here, it is shown how smaller, rocky planets tend to remain in near-circular architectures whereas larger, gaseous exoplanets deviate largely from circular.

2.3 Density Contour Predictive Modeling

In an attempt to provide a useful tool to be used by the exoplanet and astrobiology communities, predictive modeling was undertaken by means of density contours. Here, the correlation between four pairs of variables pertaining to stellar and exoplanet parameters (orbital eccentricity, planetary mass, stellar mass, and stellar metallicity) were explored

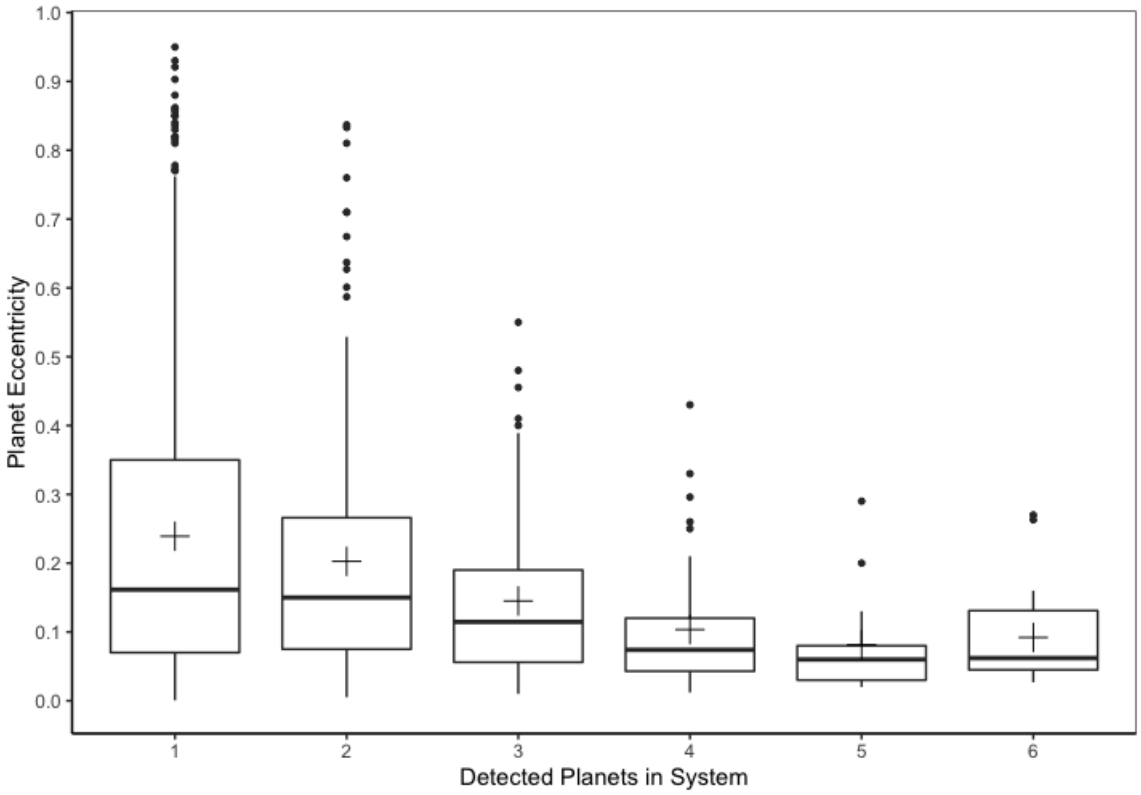

Figure 2.6 Box plots displaying exoplanet system multiplicity. Here, the box represents the interquartile range (IQR) with the bottom line being the first quartile (Q1) and the top line the third quartile (Q3). The solid line in the center of each box represents the mean value, and the cross hairs represent the median value. The bottom whisker denotes the "minimum" (Q1-1.5*IQR) and the top whisker denotes the maximum (Q3+1.5*IQR). Each point represents an outlier.

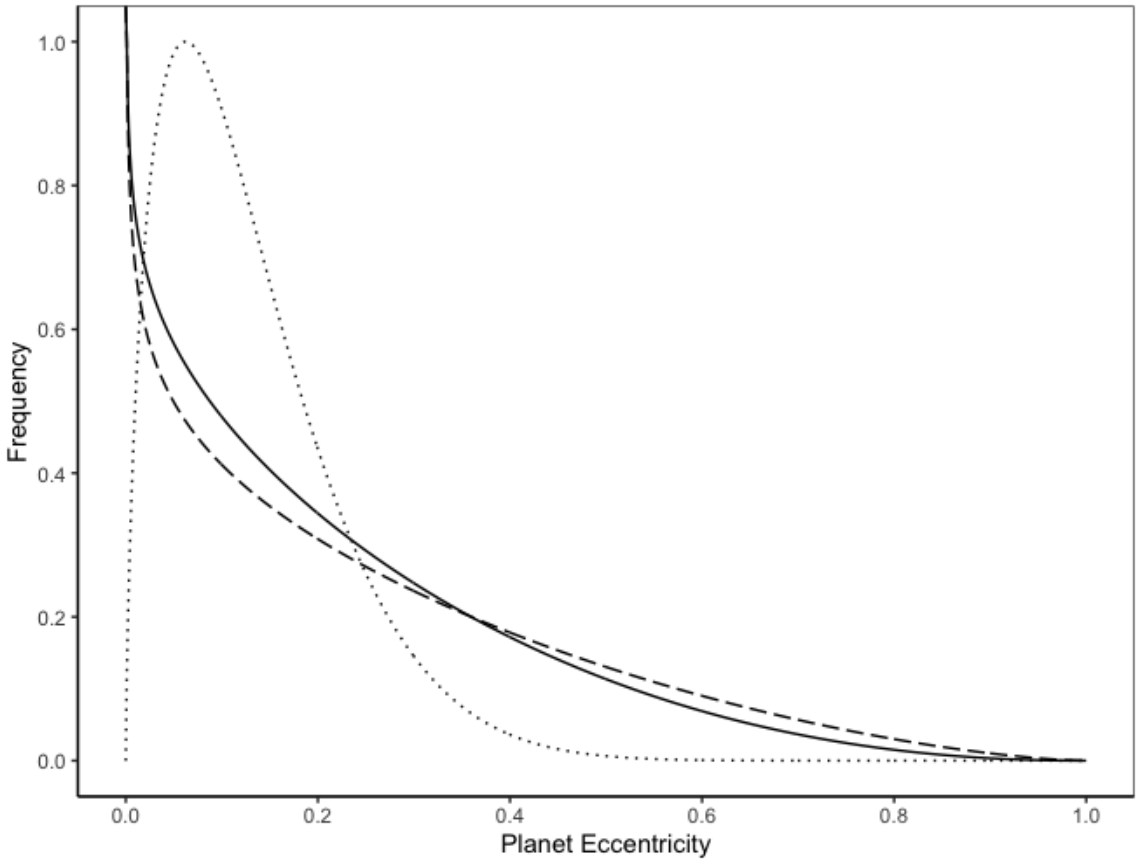

Figure 2.7 Beta-distribution fits applied to the entire exoplanet data set (solid), gaseous exoplanets (dashed), and rocky planets (dotted).

(Figures 2.8, 2.9, 2.10, and 2.11. The idea for producing these is that given one or more of the parameters represented by the y-variable, one could estimate the parameter represented by the x-variable in the absence of measurement. Within each plot, specific features which describe the data arose. Concerning figures 2.8, 2.9, 2.11, two hot spots can be found in each. The two groups highlighted by these hot spots represent the groups of rocky and gaseous exoplanets. Regarding the distributions of stellar parameters, we see that, not surprisingly, both greater stellar mass and stellar metallicity will produce larger planets as can be seen by the slight offset on the x-axis for the respective hot spots. What is less obvious is the relationship between planet eccentricity and mass shown in the top left. This clearly displays a positive correlation between the two variables where larger planets generally feature greater eccentricities. For the smaller, rocky planets, the eccentricity threshold seems to be around 0.55. That is, there are no detected rocky planets with an eccentricity greater than this value. As in the previous sections, this data strongly supports the proposed planet-planet scattering theory.

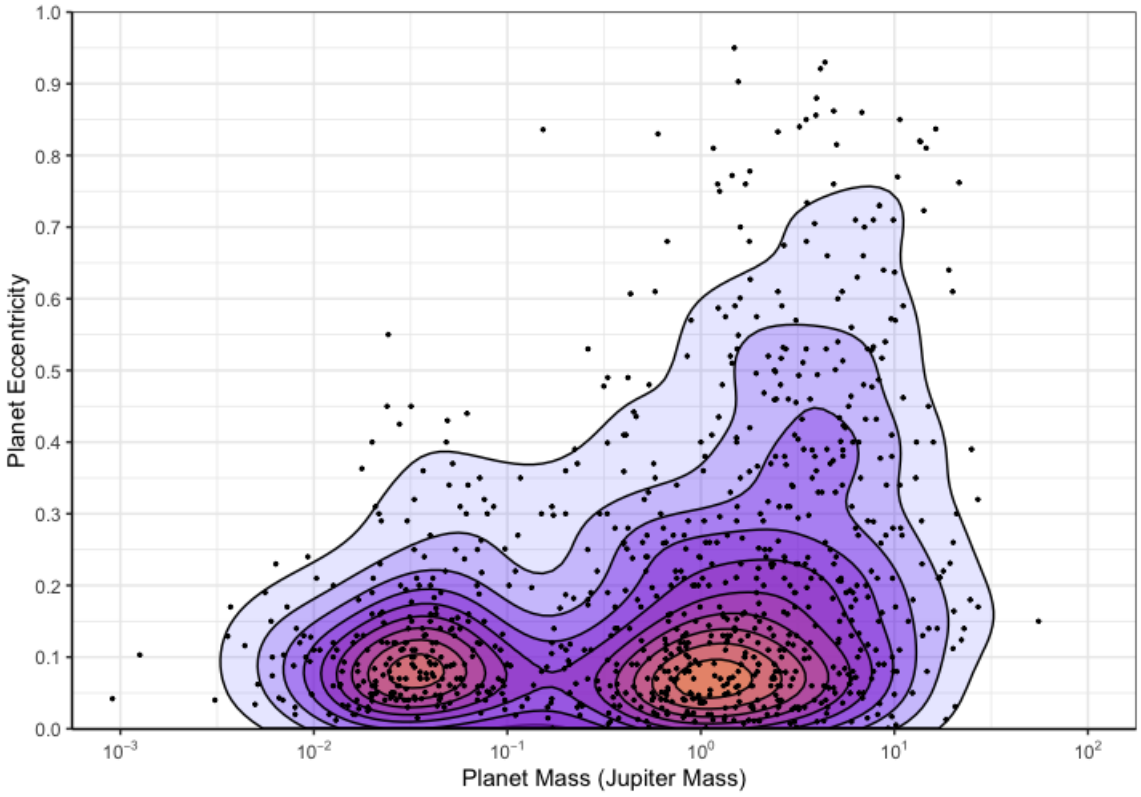

Figure 2.8 The distribution of measured planetary masses and their corresponding eccentricities (n = 890 exoplanets). Overlaid density contours indicate areas of higher density (orange hot spots) and lower density (lightest violet). Here, two hot spots appear along the x-axis. These hot spots pertain to the group of denser rocky exoplanets (left) and gassy giant planets (right).

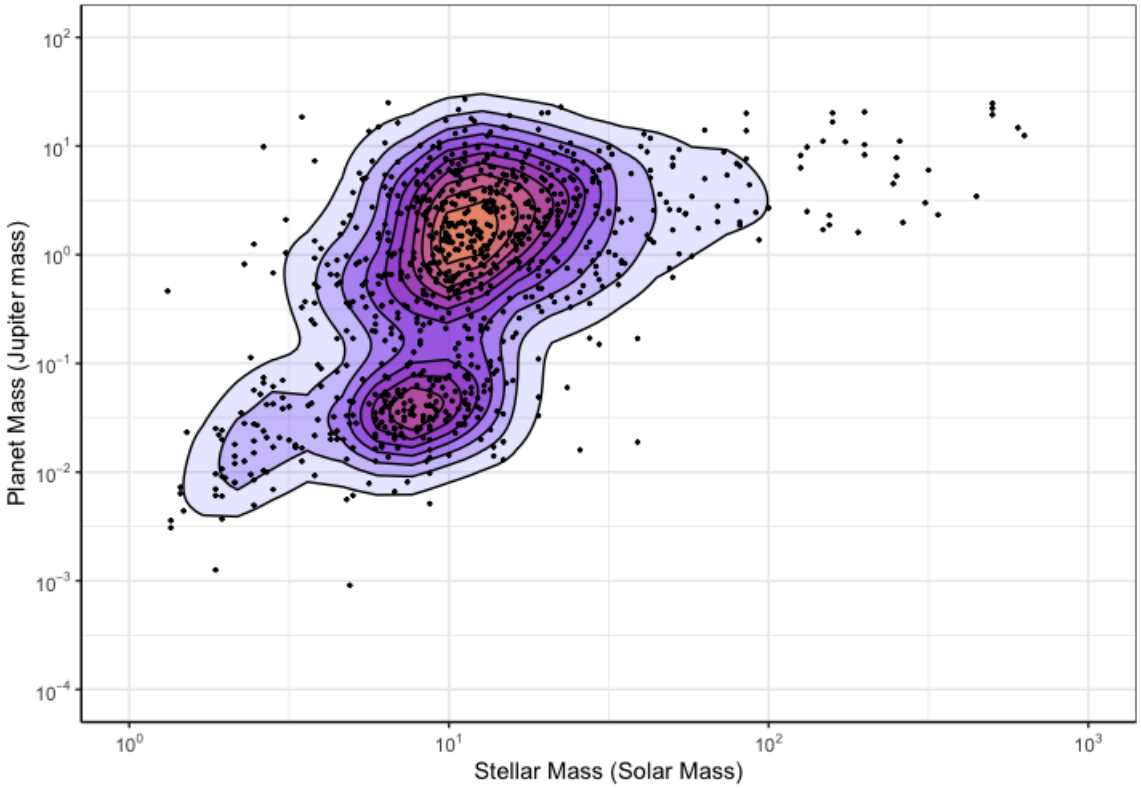

Figure 2.9 The distribution of measured planetary masses and their corresponding stellar masses (n = 890 exoplanets). Overlaid density contours indicate areas of higher density (orange hot spots) and lower density (lightest violet). Here, two hot spots appear along the y-axis. These hot spots pertain to the group of denser rocky exoplanets (top) and gassy giant planets (bottom). There appears to be a third outlier group in the top right of the scatter.

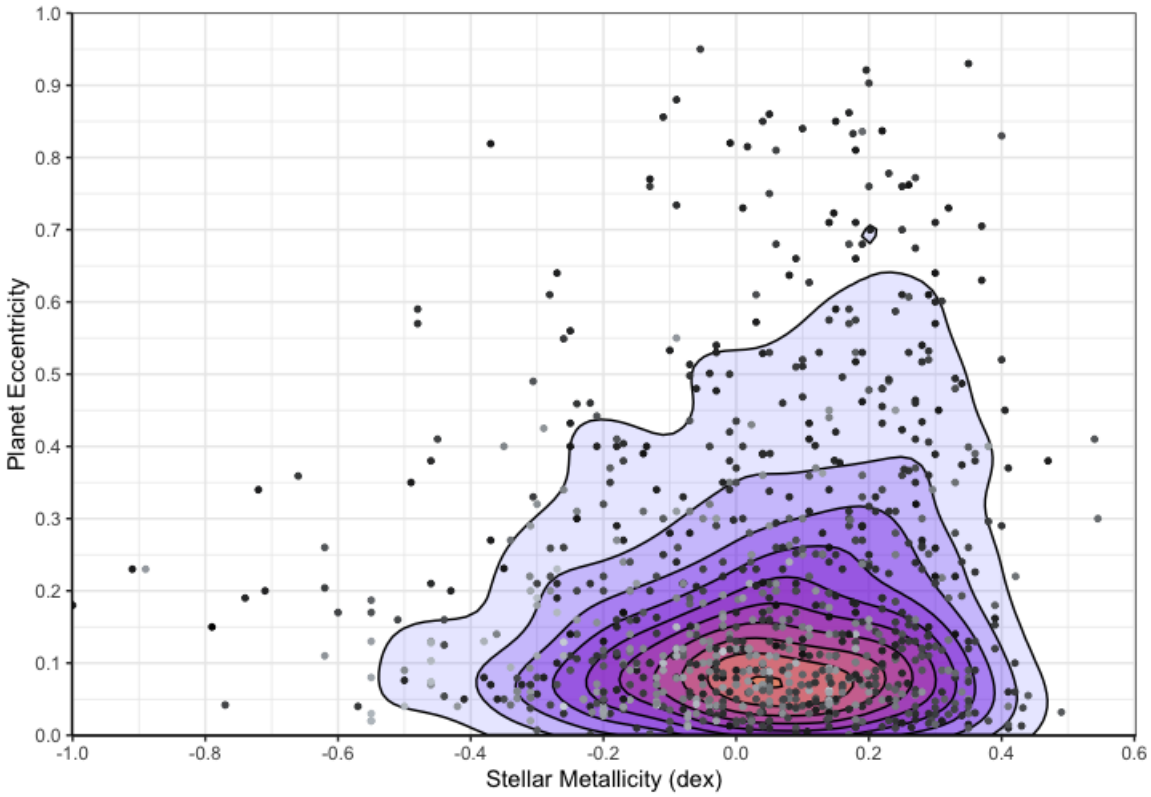

Figure 2.10 The distribution of measured planetary eccentricities and their corresponding stellar metallicities ($n = 890$ exoplanets). Overlaid density contours indicate areas of higher density (orange hot spot) and lower density (lightest violet). Here, the points are color coded by planetary mass where higher masses are darker and lower masses are lighter. Note only the higher mass planets reach the highest eccentricities, which agree with the data shown in Figure 2.8.

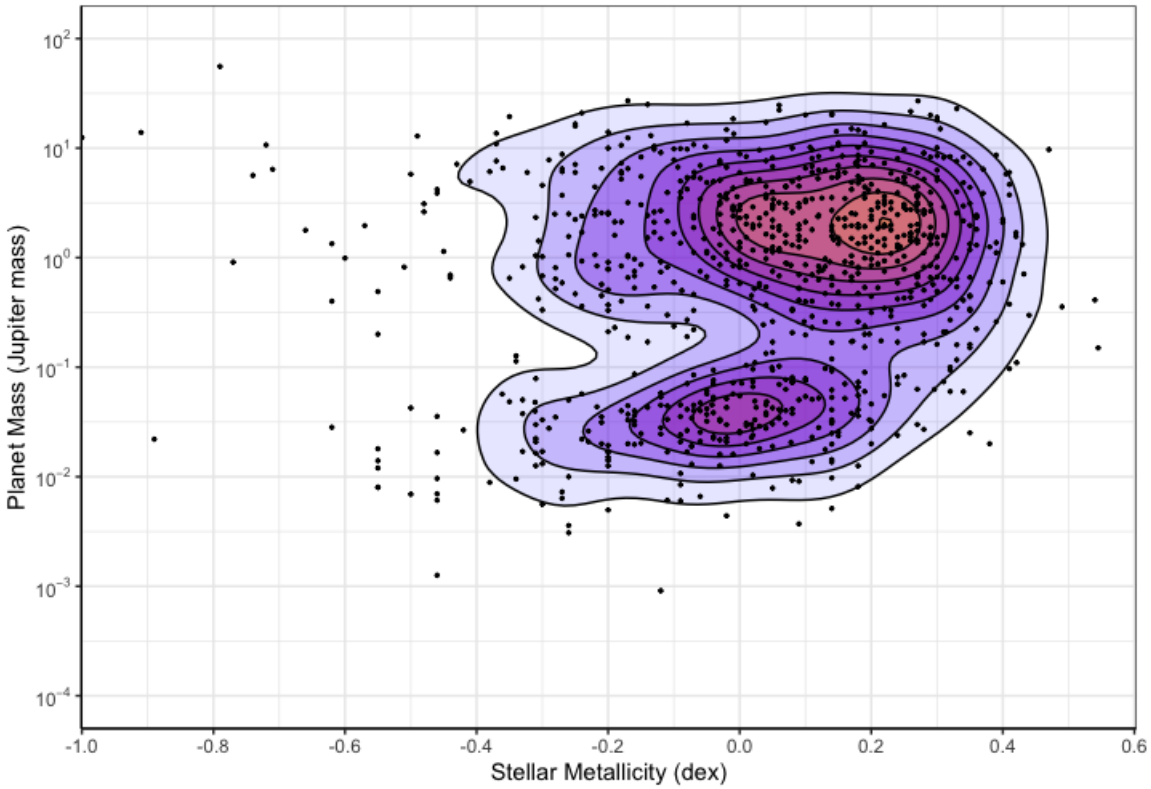

Figure 2.11 The distribution of measured planetary masses and their corresponding stellar metallicities ($n = 890$ exoplanets). Overlaid density contours indicate areas of higher density (orange hot spots) and lower density (lightest violet). Here, two hot spots appear along the y-axis. These pertain to the group of denser rocky exoplanets (bottom) and gassy giant planets (top).

Chapter 3

Discussion and Conclusions

The data presented in this work strongly supports the hypothesis that stars with greater masses and radii will have a large enough mass to hold their planets in mostly circular orbits, and that planets orbiting further from their host stars are more likely to be eccentric, supporting the planet-planet scattering theory.

The topic of eccentric orbits has interesting implications for habitability. An eccentric planet will experience the closest approach to its host star at periastron, and the furthest approach at apastron. At each of these points in its orbit, such a planet will receive the highest and lowest amount of radiative flux, respectively. At higher eccentricities, the planet will experience both a closer and further approach at periastron and apastron, producing a greater range of received flux over the entire orbital phase. Kane & Gelino (2012) showed smaller planets have smaller eccentricity. Clearly orbital eccentricity is crucial in characterizing exoplanet habitability. In addressing goals of the astrobiology community, it is of unique interest to identify the origin and nature of eccentric orbits.

In recent years, the Kepler telescope provided us with an array of exoplanet measurements which have made the proposed work possible in the context of exoplanet statistics. Although not much data was collected in regard to individual eccentricities. The TESS telescope, however, is currently measuring nearby bright stars and collecting a great deal of individual exoplanet eccentricities. The work described preesnts novel, unpublished data yielding from this mission. And, in coming years, telescopes like JWST, LuVoir, and HabEx will be used to measure atmospheres and test the specific effects of eccentricity of climates. The project described herein will undoubtedly advance the return of these planned future missions.

Bibliography

Bertrand, T., & Forget, F. 2017, Icarus, 287, 72

Bodenheimer, P., & Pollack, J. B. 1986, Icarus, 67, 391

Bowler, B. P., Blunt, S. C., & Nielsen, E. L. 2020, The Astronomical Journal, 159, 63

Carrera, D., Raymond, S. N., & Davies, M. B. 2019, Astronomy & Astrophysics, 629, L7

Chatterjee, S., Ford, E. B., Matsumura, S., & Rasio, F. A. 2008, The Astrophysical Journal, 686, 580

Dressing, C. D., Spiegel, D. S., Scharf, C. A., Menou, K., & Raymond, S. N. 2010, The Astrophysical Journal, 721, 1295

Jurić, M., & Tremaine, S. 2008, The Astrophysical Journal, 686, 603

Kane, S. R., & Blunt, S. 2019, The Astronomical Journal, 158, 209

Kane, S. R., Ciardi, D. R., Gelino, D. M., & von Braun, K. 2012, Monthly Notices of the Royal Astronomical Society, 425, 757

Kane, S. R., & Gelino, D. M. 2012, Astrobiology, 12, 940

Kane, S. R., & Raymond, S. N. 2014, The Astrophysical Journal, 784, 104

Kane, S. R., & Torres, S. M. 2017, The Astronomical Journal, 154, 204

Kane, S. R., Wittenmyer, R. A., Hinkel, N. R., et al. 2016, The Astrophysical Journal, 821, 65

Kipping, D. M. 2013, Monthly Notices of the Royal Astronomical Society: Letters, 434, L51

Liu, M. C., Magnier, E. A., Deacon, N. R., et al. 2013, The Astrophysical Journal Letters, 777, L20

Luhman, K., Adame, L., D'Alessio, P., et al. 2005, The Astrophysical Journal, 635, L93

Mills, S. M., Howard, A. W., Petigura, E. A., et al. 2019, The Astronomical Journal, 157, 198

Mizuno, H., Nakazawa, K., & Hayashi, C. 1978, Progress of Theoretical Physics, 60, 699

Mordasini, C., Alibert, Y., Benz, W., & Naef, D. 2007, arXiv preprint arXiv:0710.5667

Nielsen, E. L., De Rosa, R. J., Macintosh, B., et al. 2019, The Astronomical Journal, 158, 13

Perri, F., & Cameron, A. G. 1974, Icarus, 22, 416

Perryman, M. 2018, The exoplanet handbook (Cambridge university press)

Shen, Y., & Turner, E. L. 2008, The Astrophysical Journal, 685, 553

Van Eylen, V., Albrecht, S., Huang, X., et al. 2019, The Astronomical Journal, 157, 61

Way, M. J., & Georgakarakos, N. 2017, The Astrophysical Journal Letters, 835, L1

Wilson, D., Gillon, M., Hellier, C., et al. 2008, The Astrophysical Journal, 675, L113